Received: 11 March 2020 | Revised: 18 June 2020 | Accepted: 8 July 2020

DOI: 10.1002/aic.16928

TRANSPORT PHENOMENA AND FLUID MECHANICS

AIChE JOURNAL

Computational evaluation of effective transport properties of differential microcellular structures

Abdulrazak J. Otaru[1] | Mukhtar Abdulkadir[1] | Martin R. Corfield[2] | Anatole Kenfack[3] | Nuradeen Tanko[4]

[1]Department of Chemical Engineering, Federal University of Technology, Minna, Niger State, Nigeria

[2]Department of Electrical and Electronic Engineering, The University of Nottingham, Nottingham, UK

[3]African University of Science and Technology, Abuja, Nigeria

[4]Department of Petroleum and Natural Gas Engineering, Baze University, Abuja, Nigeria

Correspondence
Abdulrazak J. Otaru, Department of Chemical Engineering, Federal University of Technology, P.M.B. 065, Gidan-Kwanu Campus, Bida Road, Minna, Niger State, Nigeria.
Email: otaru_12257@yahoo.com

Abstract

This study presents a combined implementation of three-dimensional (3D) advanced imaging and computational fluid dynamics (CFD) modeling and simulation techniques to interpret the effective transport properties of single and stacked samples of differential microcellular structures. 3D morphological analysis software (ScanIP) was used to create representative elemental volumes via high-resolution tomography data for samples of *tetrakaidekahedron-shaped* Inconel and *bottleneck-type* aluminum foams. Pore-structure-related information for single and stacked differential samples were obtained with the aid of image analysis software, while their effective transport properties were attained by computationally resolving the pressure drop developed across these materials for superficial fluid velocities in the range from 0 to 6 m s^{-1}. Model validation was demonstrated by tolerable agreement between resulting CFD predicted results and experimentally measured values of flow properties. With these techniques, contributory effects were identified for pore-structure-related properties, pore density, and flow entrance on the flow dynamics of microcellular structures. This approach could prove useful in the design of highly efficient porous metallic components for applications specific to fluid transport.

KEYWORDS

advanced imaging, CFD, porous metallic structures

1 | INTRODUCTION

Cellular metallic structures are classified as load-bearing and multifunctional materials which are attributable to their attractive mechanical, vibrational, lightweight (low-density), electrical, corrosion resistance and fluid transport with excellent mixing properties.[1-5] Porous metallic structures are widely classified into open-celled and close-celled cellular materials with no moving parts (control pore network and distinctive pore volume) resulting in comparatively simple and less frequent maintenance. While the close-celled cellular structures are cited to offer high resistance to fluid flow due to their low pore volume,[5-7] the open-celled cellular structures are characterized by higher open porosity, random topologies with greater accessible surface area per unit volume or specific surface.[8-10] Typical applications of porous metallic structures are in the fabrication of reactors, heat exchangers, aero-engine fuel separators, vibrational and emission control in cars, lightweight solar collectors, fuel cells, and biomedical devices.[3,4,6] Porous metallic filters are also utilized in the design and fabrication of oil and gas industrial equipment, most especially, as a catalyst and product recovery in gas catalytic reactions (downstream sector) and in the screening of sands from heavy oil, that is, steam-assisted gravity challenge in the upstream sector.[11] Figure 1 presents scanning electron microscopy (SEM) and optical images of porous aluminum foams showing typical pore morphology, pore sizes, pore openings, joints, and ligaments.[12]

Fluid flow applications for porous metallic structures generally require understanding, estimation, and optimization of their flow permeability (capacity of a porous material for transmitting a fluid) and

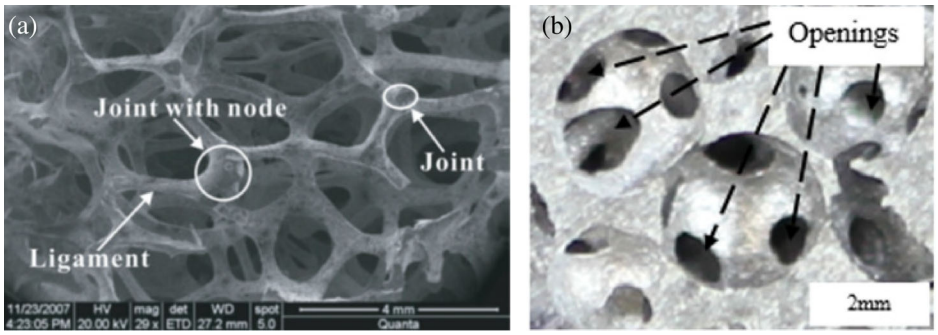

FIGURE 1 (a) Scanning electron microscopy (SEM) of high porosity (ε ~ 0.92) *tetrakaidekahedron-shaped* (adapted from Reference 12), and (b) optical micrograph of *bottleneck-type* porous metallic structures showing typical surface morphology (adapted from Reference 13) [Color figure can be viewed at wileyonlinelibrary.com]

Form (pressure) drag information. These properties can be obtained by fitting measured unit pressure drop data (pressure drop per unit sample thickness) developed for flowing fluids across the interstices of a porous matrix into the well-known Darcy (Equation (1)) and Darcy–Dupuit–Forchheimer (Equation (2)) models. Darcy flow regimes of fluid are characterized by viscous-dominated fluids or for very slow fluid velocities, typically, for pore diameter Reynolds number (R_D) below unity.[4,14] Experimental, numerical modeling, and simulation in Reference 3 indicates that nonlinearity effects dominate fluids at very high velocities, typically in the fully laminar (Forchheimer) and turbulent flow regimes thereby giving greater significance to the Form drag, over permeability, in describing accurately fluid transport across porous structures. These separated flow regimes are delineated in Reference 15 using dimensionless pressure gradient, η (Equation (3)) against pore diameter Reynolds number. Though, the dimensionless friction factor, f (Equation (3)) has been widely quoted for delineating flow regimes in packed bed of structures[16-18] for decades. Similarly, there are applicable theories for the dimensionless friction factor in separating flow regimes in porous metallic structures.

$$\nabla P = \frac{\mu}{k_o} u_{s,} \tag{1}$$

$$\nabla P = \frac{\mu}{k_o} u_s + \rho \frac{C_F}{\sqrt{k_o}} u_s^2 \left(C_F = C\sqrt{k_o}, R_D = \frac{\rho u_s D_p}{\mu} \right), \tag{2}$$

$$\eta = \frac{\nabla P \cdot D_p^2}{\mu u_s} \text{and} f = \frac{\Delta P}{\frac{1}{2}\rho u_s^2}, \tag{3}$$

where ΔP is the pressure drop across a porous sample (Pa), u_s is the superficial fluid inlet velocity (m s^{-1}), ∇P is the unit pressure drop per unit sample thickness (Pa m^{-1}), k_o is the permeability of the porous medium (m^2), C is the Form drag (m^{-1}), C_F is the dimensionless Forchheimer coefficient (–), ρ is the fluid density (kg m^{-3}), μ is the dynamic fluid viscosity (Pa s), D_p is the mean pore diameter size of the porous structure, η is the nondimensional pressure gradient (–), R_D is the nondimensional Reynolds number (–), and f is the dimensionless friction factor (–). The resultant pressure drop developed for moving fluids across these porous matrices is mainly dependent on their pore morphological properties, typically, their pore openings, pore sizes, and pore volume. Studies in References 6 and 19 varied the pore-structure-related properties and topology of these materials through compression thereby changing the pore-structure-related properties. The recorded values of unit pressure drop developed across compressed materials were reportedly higher than for uncompressed structures.

The determination of pressure drop across porous structures is often carried out with the aid of experimental setup apparatus involving the use of flow meters and digital manometers and/or connected pressure transducers for obtaining the superficial fluid velocity and differential pressure drop, respectively.[19-22] While there is little or no doubt in the validity and reliability of well-conducted experimental works within the field of transport in porous media, it does, however, require significant amounts of funding for a full economic costing. A pore-scale computational modeling approach has a somewhat economic advantage over experimentation and has attracted interest from leading researchers in this field. In addition, this technique is reported[23] to yield better computational results (than medium-scale simulation) due to its ability to capture detailed and accurate information of porous structures with less computational demand, consuming less time and resources when compared to large-scale numerical simulations.[13,23]

Several authors[3-5,10,12,13,15-18,22,24] in the field of transport in porous media maintain that the implementation of molecular-dynamic equations and fundamental flow equations at the pore level is fundamental for a better understanding of the flow dynamics developed across porous media. Analogous research work has seen the utilization of X-ray micro-computed tomography (μCT) and virtual packing of structures to accurately represent the pore morphology of porous metallic structures. Ranut et al[15] adopted the pore-scale technique using tomography data sets to account for the permeability and Form drag of highly porous metals with reasonable fits to experimentally measured data. The contributory effects imposed by pore sizes and pore openings on the pressure drop developed across *bottleneck-type* microcellular structures are described in References 4, 21, and 22. Della Torre et al[24] described the combined utilisation of image processing and computational fluid dynamics (CFD) modeling and simulation to account for the flow properties of highly porosity metal foams. This led to a proposed formulation that relates the permeability of the porous structures as a function of their pore morphological properties, which is independent of their fluid properties. A virtual representation of the Kelvin-cell lattices was adopted in Reference 25

to create a semblance of *tetrakaidekahedron-shaped* porous matrices to account for gas transport and catalytic reactions occurring over the surface of a highly porous metallic material. Three-dimensional (3D) advanced image processing, computational fluid dynamics modeling and simulation of fluid flow across low-porosity (60–70%) virtual structures were described in Reference 26 to account for the permeability of *bottleneck-type* microcellular structures. This approach[26] enabled an understanding of the dependence of flow permeability on the pore-structure-related properties (most importantly, the pore diameter openings) of the porous structures. The results of μCT-based CFD modeling and simulation of fluid transport across differential open-celled aluminum foams were reported in Reference 27 for laminar flow regimes.

Several other researchers in References 28–35 also used μCT-based pore-scale CFD modeling and simulation approach to fully described the flow behavior in porous metallic structures with reasonable correlation to experimentally measured data. Despite the numerous applications of a μCT-based pore-scale CFD approach to fully described the fluid dynamics across these microcellular structures, flow studies have been limited to single samples at a time, with little or no information on CFD of fluid flow across stacked samples for these structures. In addition, the impact of flow entrance on stacked samples of *bottleneck-type* structures has not yet been fully explored. This work, therefore, seeks to investigate the fluid flow behavior characterized by single and stacked samples of differential *tetrakaidekahedron-shaped* Inconel and *bottleneck-type* aluminum (Al) porous metals (produced by a replication casting process) using 3D X-ray CT imaging; determination of the pore-structure-related properties of the porous metals; modeling of the pressure drop across representative single and stacked samples on the microstructural level, with corresponding experimental measurements of pressure drop across these samples.

2 | RESEARCH APPROACH

Two-dimensional (2D) X-ray tomography cross-sectional images of Inconel 450 μm (*A*), Inconel 1,200 μm (*B*), aluminum (*X*), and aluminum

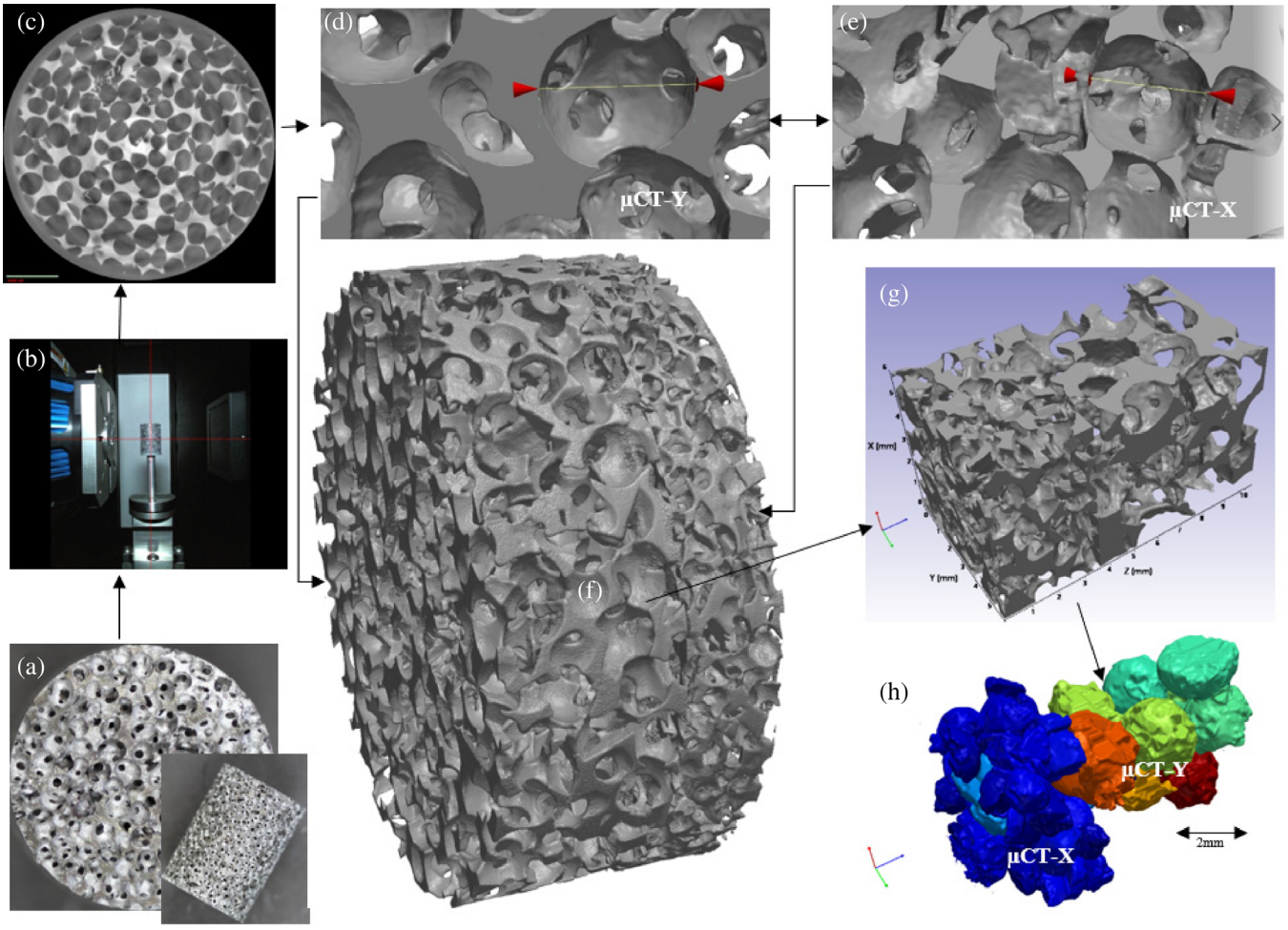

FIGURE 2 Micro-computerized tomography (CT) reconstructed *X*–*Y* "bottleneck-type" structures: (a) optical images of a *bottleneck-type* structure, (b) internal view of a X-radia 500 tomography system showing sample of metallic foam mounted on a sample stage with X-ray source and detector visible. (c) Representative two-dimensional tomography data set/slice. (d) Internal view of the reconstructed three-dimensional (3D) structure showing typical pore size and openings for the *Y* sample and (e) *X* samples. (f) Reconstructed 3D volume of the stacked samples *X*–*Y*, (g) 3D reconstructed represented elemental volume (REV), and (h) 3D watershed segmented particles of stacked *X*–*Y* sample of *bottleneck-shaped* aluminum foams [Color figure can be viewed at wileyonlinelibrary.com]

(*Y*) foams were obtained via a Zeiss Xradia Versa XRM-500 3D X-ray CT microscopy system. The Inconel foams were produced by Alantum Company, an innovation in alloy foams, while the *bottleneck-type* Al foams were produced by a replication casting route.[22,23,36]

μCT reconstruction process for aluminum foam samples *X* and *Y* were achieved by mounting individual sample (Figure 2a) on the sample stage of a Zeiss Xradia Versa XRM-500 3D X-ray CT microscopy system, as shown in Figure 2b. A combination of geometric and optical (two-stage) magnification was used to achieve high-resolution, typically, 26-μm scan[37,38] using 1,600 projected images. 2D slices (Figure 2c) in tagged image file format (Tiff) corresponding to the 3D spatial geometry (obtained from the reconstructed tomography slices) were transferred to ScanIP module of Synopsys-Simpleware™ for processing, pore-structure characterization and image discretization. Image editing using tools such as masking, thresholding, smart mask filtering, erosion, dilation, and so on available within the ScanIP module were employed to reconstruct a 3D volume (Figure 2f) and a 3D workable representative elemental volume (REV). The 3D REV sample was characterized by a sample thickness that is 3–5×, its mean pore size (in the direction of fluid flow, ZZ) with a less than 2% difference when compared to its initial bulk value, typically giving an *XX*, *YY*, *ZZ* 3D RVE dimension $6 \times 6 \times 8$ mm. Pore structural characterization of the 3D REV sample was done within the ScanIP to account for its pore volume, pore volume fraction, specific surface (surface area per unit volume), mean pore size, and mean pore openings. The first three properties were measured directly while the mean pore openings and mean pore sizes (Figure 2h) were measured by utilizing the centerline statistical tools and watershed segmentation of a Boolean inverted 3D REV (fluid volume) sample, respectively. This approach was repeated for the individual samples of the Inconel foams. In addition, stacked samples of reconstructed 3D REV *X*–*Y* (Figure 2g) and *A*–*B* structures were achieved using image processing of selected tomography scans of different sample slices combined. It is important to note that the image resolution for the Inconel structures was 12 μm while the image resolution for the porous aluminum foams was 26 μm. The tolerable deviations between the porosities of the real and μCT reconstructed samples are an indication that the image resolutions are high enough to give an accurate description of the materials pore network.

A likely trade-off in mesh counts and accuracy was done (using simulation approaches reported in References 3 and 22) by finding a workable mesh balance capable of converging faster while maintaining tolerable deviations between CFD-modeled and experimentally measured data. A linear tetrahedral mesh structure with a growth rate of 1.3 was adopted to discretize the fluid domain of the 3D REV porous structures (in the +FE module of Synopsys-Simpleware™) into smaller cell sizes that is ×1.5–6.5 image resolution of respective samples mesh sizes, yielding an optimum mesh structure characterized by cell density ranging between 2.5 and 4.5 M cells. Preliminary observations show that the effect of increasing mesh density beyond this limit only improves accuracy by 0.2%. However, the excessive computational demand and longer runtime needed to resolve a single solution of pressure drop value within the available PC specification (64 GB RAM) resulted in the trade-off of this tolerable margin. The CFD package of COMSOL Multiphysics™ was used to resolve the physics of fluid developed across these materials for superficial inlet fluid velocities ranging from 0 to 6 m s^{-1}. The compressible flow Navier–Stokes equation was solved on the 3D REV fluid domain while the inlet and outlet sections of the porous structures were conditioned to velocity inlet and zero pressure outlet, respectively. A symmetrical boundary condition was selected for the four side faces while the skeletal frame was conditioned to represent cell walls. The selected physics and boundary conditions were selected for all samples, most especially, for fluid superficial inlet velocities below 5.0 m s^{-1}, this is within the laminar flow regime ($R_D \leq 300$[24,39]). The Algebraic yPlus Reynolds Average Navier–Stokes model was solved for higher fluid velocities ($u_s \geq 5$ m s^{-1}) to account for the eddy viscosities that augment the molecular viscosity as the fluid propagates the interstices of the porous matrix.

Experimental measurements of the pressure drop developed for a flowing fluid across the samples were determined using the experimental setup, as shown below (Figure 3), as described in References 22, 23, and 40. In brief, porous metallic structure is placed in the mid-assembly (sample holder). Compressed air is passed through a pressure filter regulator to the mid-assembly via a flow straightener. The flow rate (in liters per minute [LPM]) was measured via a Flo-Rite™ flow meter while the voltage drop across the sample was taken with the aid of a Gems pressure transducer connected to LabView™. Time-series voltage data were taken for each recorded fluid flow rate (14-95LPM) with a stabilization period of 2–3 min. Initial voltage–pressure calibrations and repeatability analysis were carried out to ensure accuracy and to minimize experimental error. A greater coefficient of friction between the sample and internal diameter of the mid-flange assembly was ensured by wrapping the cylindrically shaped boundary of the sample with polytetrafluoroethylene tape. Compressibility effects were taken into consideration (using compressibility equation in References 2, 22, 23, and 41) to account for the changes in fluid density and to avoid any underestimation of the static pressure variation resulting from fractional volume changes in a moving fluid (compressed air). The pressure drop developed across all single and stacked samples of porous metals were measured using approach, as discussed above.

3 | ANALYSIS OF RESEARCH DATA

The results obtained from the experimentally measured and μCT-based CFD modeled data are presented in Figure 4. Table 1 presents μCT-based pore-structure-related and effective transport properties obtained for the single, stacked, and structurally adapted samples (to be discussed later) of differential microcellular structures. The unit pressure drop recorded for both the Inconel and Al foams fit well into the second-order Darcy–Dupuit–Forchheimer polynomial model (Equation (2)) with a correlation coefficient of approximately one. The pore structure-related properties recorded in Table 1 are mean pore diameter size (D_p), mean pore openings (D_w), foam porosity (ε), surface

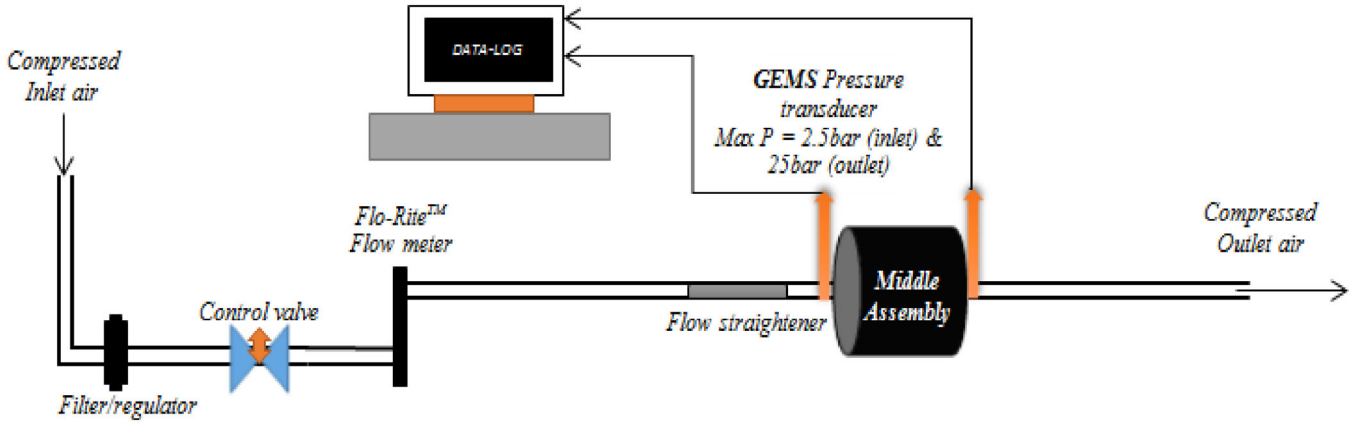

FIGURE 3 Schematic representation of airflow measurement (adapted from Reference 22) [Color figure can be viewed at wileyonlinelibrary.com]

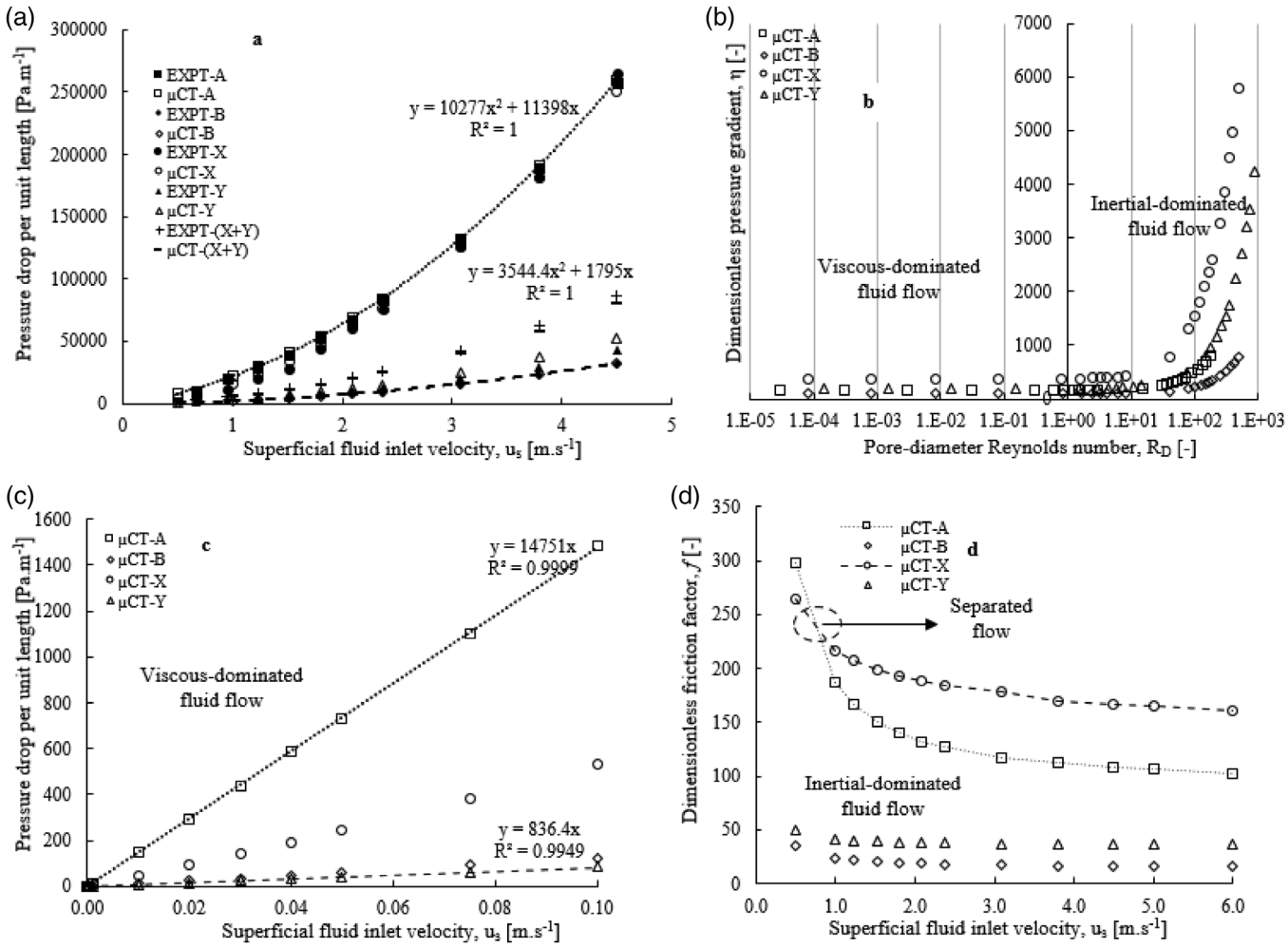

FIGURE 4 Graphical representations of flow information of single samples of porous metallic structures. (a) Experimentally measured and computational fluid dynamics (CFD) modeled data of unit pressure drop, ∇P (Pa m^{-1}) against superficial fluid inlet velocity, u_s (m s^{-1}), (b) dimensionless pressure gradient, η (–) against pore diameter Reynolds number, R_D (–), (c) unit pressure drop, ∇P (Pa m^{-1}) against superficial fluid velocity, u_s (m s^{-1}) in the viscous-dominated regime and (d) dimensionless friction factor, f (–) against superficial fluid inlet velocity, u_s (m s^{-1}) in the inertial dominated regime

area per unit bulk volume (σ_{FB}), and surface area per unit structure (material) volume (σ_{FF}). In addition, effective transport properties obtained from the pressure drop developed across the porous samples are viscous-dominated flow permeability (k_0), inertial-dominated flow permeability (k_i), Form drag (C) and dimensionless Forchheimer coefficient ($C_F = C/\sqrt{k_0}$). Figure 4a shows close

TABLE 1 Pore-structure-related and flow information for the single and stacked samples of Inconel and *bottleneck-type* porous metallic structures

X-ray micro-computed tomography samples (μCT)	Mean pore sizes, D_p (mm)	Mean openings, D_w (mm)	Porosity, ε (%)	Specific surface, σ_{FB} (mm^{-1})	Specific surface, σ_{FF} (mm^{-1})	Permeability $k_0/10^{-09}$ (m^2) (Darcy)	Permeability $k_i/10^{-09}$ (m^2, inertial)	Permeability, $k/10^{-09}$ (m^2, all regimes)	Form Drag C (m^{-1}, all regimes)	Form Drag C_F (–, all regimes)
Inc 450 μm—*A*	0.450	0.239	83.543	8.626	43.817	1.249	1.601	1.601	8,541.546	0.342
Inc 1,200 μm—B	1.230	0.489	90.621	3.216	31.095	15.562	22.639	22.639	1,183.946	0.178
Al foam 1—*X*	1.213	0.275	72.093	4.588	12.294	3.868	2.856	2.856	9,076.119	0.485
Al foam 2—*Y*	2.226	0.899	78.218	2.054	7.456	24.607	37.618	37.618	2080.103	0.403
1LA + 1LB	0.662	0.322	85.349	7.869	36.230	1.946	2.455	2.455	6,155.308	0.305
1LB + 1LA	0.662	0.322	85.349	7.869	36.230	2.097	2.651	2.651	5,923.383	0.305
2LA + 1LB	0.573	0.289	84.381	7.019	37.940	1.632	2.112	2.112	6,919.980	0.318
1LA + 1LB + 1LA	0.573	0.289	84.471	7.869	36.230	2.097	2.316	2.316	5,764.589	0.277
1LA + 1LB (ER1)	0.541	0.251	76.129	7.142	36.662	0.799	0.808	0.808	14,532.249	0.413
1LA + 1LB (ER2)	0.458	0.182	67.211	8.110	37.077	0.284	0.198	0.198	41,485.847	0.584
1LA + 1LB (ER3)	0.388	0.132	58.687	9.322	37.234	0.091	0.048	0.048	121,520.711	0.844
X + *Y*	1.719	0.674	74.781	3.077	9.122	9.290	8.904	8.904	2,973.080	0.271
Y + *X*	1.719	0.674	74.781	3.077	9.122	7.888	6.770	6.770	5,376.691	0.442
X + *Y* (ER1)	1.669	0.644	67.202	3.688	7.555	5.414	3.009	3.009	4,644.476	0.255
X + *Y* (ER2)	1.620	0.594	59.689	4.266	6.318	1.590	1.451	1.451	7,481.033	0.285
X + *Y* (DL1)	1.771	0.714	81.823	2.427	10.922	19.125	24.068	24.068	1,526.189	0.237
X + *Y* (DL2)	1.829	0.774	87.836	1.783	12.889	37.445	52.719	52.719	767.652	0.176

Note: A = Inconel 450 μm foam, *B* = Inconel 1,200 μm foam, *X* and *Y* are *bottleneck* aluminum foams. NB: thickness 1LA = 2.504 mm, 2LA = 5.008 mm, 1LB = 2.556 mm, *X* = 3.638 mm, *Y* = 6.679 mm.
Abbreviations: DL, dilation; ER, erosion.

TABLE 2 Experimental and CFD modeled data for the samples of porous structures for fluid flow velocity between 0.5 and 4.5 m s^{-1}

Samples	Permeability $k_0/10^{-09}$ (m^2)	Form Drag C (m^{-1})	Samples	Permeability $k_0/10^{-09}$ (m^2)	Form Drag C (m^{-1})
EXPT-*A*	1.69	8,566.4	EXPT-*Y*	35.61	1928.1
μCT-*A*	1.60	8,541.5	μCT-*Y*	37.62	2080.1
EXPT-*B*	20.67	1,162.4	EXPT- (*X* + *Y*)	9.40	3,174.6
μCT-*B*	22.64	1,183.9	μCT-*B* – (*X* + *Y*)	8.90	2,973.1
EXPT-*X*	3.06	9,181.5			
μCT-*X*	2.86	9,076.1			

Abbreviation: CFD, computational fluid dynamics.

agreement between experimentally measured and CFD-modeled data of unit pressure drop against superficial fluid velocity for both single and stacked samples of porous structures. The μCT-based CFD flow permeability and Form drag recorded for stacked samples of aluminum foams (*X* + *Y*) at superficial fluid inlet velocities in the range 0.5 and 4.5 m s^{-1} are 8.9×10^{-09} m^2 and 2,973.1 m^{-1}, respectively. The experimentally measured values of (*X* + *Y* stacked samples) flow permeability and Form drag are $9.4 \pm 0.3 \times 10^{-09}$ m^2 and 3,174.6 ± 95 m^{-1}, for the range of fluid velocities; showing a 5.0 and 6.3% deviation respectively. Similarly, a less than 7% negligible difference between the modeled and experimentally measured data for fluid flow across the single samples were obtained in Figure 4a and Table 2.

Figure 4a shows that the unit pressure drop developed across the Inconel 450 μm (*A*) and Al foam (*X*) samples are higher than for corresponding Inconel 1,200 μm (*B*) and Al foam (*Y*) samples. A rationalization of this observation was supported by plotting dimensionless pressure gradient, η (using Equation (3)) against pore diameter Reynolds number (R_D) as shown in Figure 4b, classifying the fluid flow pattern/flow regime from viscous-dominated to inertial-dominated flows. Figure 4b shows that the viscous-dominated fluid flow is characterized by little or no change in pressure gradient and flow behavior is largely controlled by the topology of the pore network.[9,14,31] Observably, precipitous changes in the dimensionless pressure gradient were consistent with inertial-dominated fluid flow, for all samples, where this regime is largely characterized by high fluid velocities caused by the presence of eddies and a greater frictional force existing between the moving fluid and pore walls of the porous matrices. An understanding of the dependence of flow permeability and Form drag on the pore-structure-related properties of the porous materials was achieved through Figures 4c,d. These figures present plots of viscous-dominated unit pressure drop (Figure 4c) and inertial-dominated dimensionless friction factor (Figure 4d) against superficial fluid inlet velocity. Figure 4c shows that the pressure drop in the Darcy flow regime is highest for the Inconel 450 μm (μCT-*A*) and lowest for the *bottleneck-shaped* Al foam (μCT-*Y*) porous structure; attributable to the changes in the macroscopic properties of the materials. Smaller pore-sized structures (μCT-*A*) lead to low Reynolds number, thereby, restricting the moving fluid to a viscous-dominated flow.[42] Table 1 shows that permeability of the porous matrices consistently decreases with decreasing pore openings and pore sizes, highlighting the fact that permeability becomes zero as either of these two parameters approaches zero. Similarly, the two specific surfaces (σ_{FF} and σ_{FB}) decrease with increasing pore size, thereby increasing the contribution of inertial forces to the pressure drop developed across the interstices of the porous structures.

Figure 4d shows that the behavior of fluid for high fluid velocities varies differently from flow manifestations in the viscous-dominated region. The contributory effects of frictional forces existing between the moving fluid and pore walls were evidently highest for the Al foam (μCT-*X*) and lowest for the Inconel 1,200 μm (μCT-*B*) sample. Intriguingly, these are the samples characterized by having the lowest and highest pore volume fraction respectively, as presented in Table 1. The Inconel 450 μm (μCT-*A*) foam may be characterized by having the higher pore density (Pores Per Inch), but the recirculatory movement of fluid at the scale boundaries of the low-porosity *bottleneck-shaped* Al foam (μCT-*X*) could be a major factor and responsible for the relative higher frictional forces characterized by moving fluid in this sample.[43] Thus, a region of separated flow is observed in Figure 4d, which exists at a velocity of 0.76 m s^{-1}; below this velocity, the flow behavior of these materials is observed to be mainly dependent on their mean pore openings. Additionally, observations from the μCT-based CFD raw data obtained for the *tetrakaidekahedron-shaped* Inconel 1,200 μm (*B*) and *bottleneck-shaped* Al foam (μCT-*Y*) also show that a region of separated flow exists at a superficial fluid inlet velocity of 0.2 m s^{-1}. The Inconel 1,200 μm (*B*) foam may be characterized by having the higher pore volume fraction (Table 1) but the larger pore openings characterized by the low-porosity Al foam (μCT-*Y*) enables higher flow passage at Darcy velocities, where permeability is key in describing the flow behavior of this material.[14] This is evident from Table 1 where the flow permeabilities are 22.64×10^{-09} and 37.62×10^{-09} m^2 for the Inconel 1,200 μm and Al foam (μCT-*Y*) samples, respectively.

Figure 5 presents 3D pressure streamline/arrow plots for (a) Inconel 450 μm (μCT-*A*), (b) Inconel 1,200 μm (μCT-*B*), (c) Al foam (μCT-*X*), and (d) Al foam (μCT-*Y*) porous metallic structures computed at a superficial fluid inlet velocity of 1 m s^{-1}. As expected, pressure values recorded in the representative pressure plots were highest at the inlet and indicate that pressure drop decreases in the direction of the moving fluid[40]. The pressure drop developed across the sample with the highest pore density structure (μCT-*A*) is relatively high and at a maximum for the Al foam (*X*). Porous metallic samples in Figure 5b,d are characterized by a lower pore density resulting in

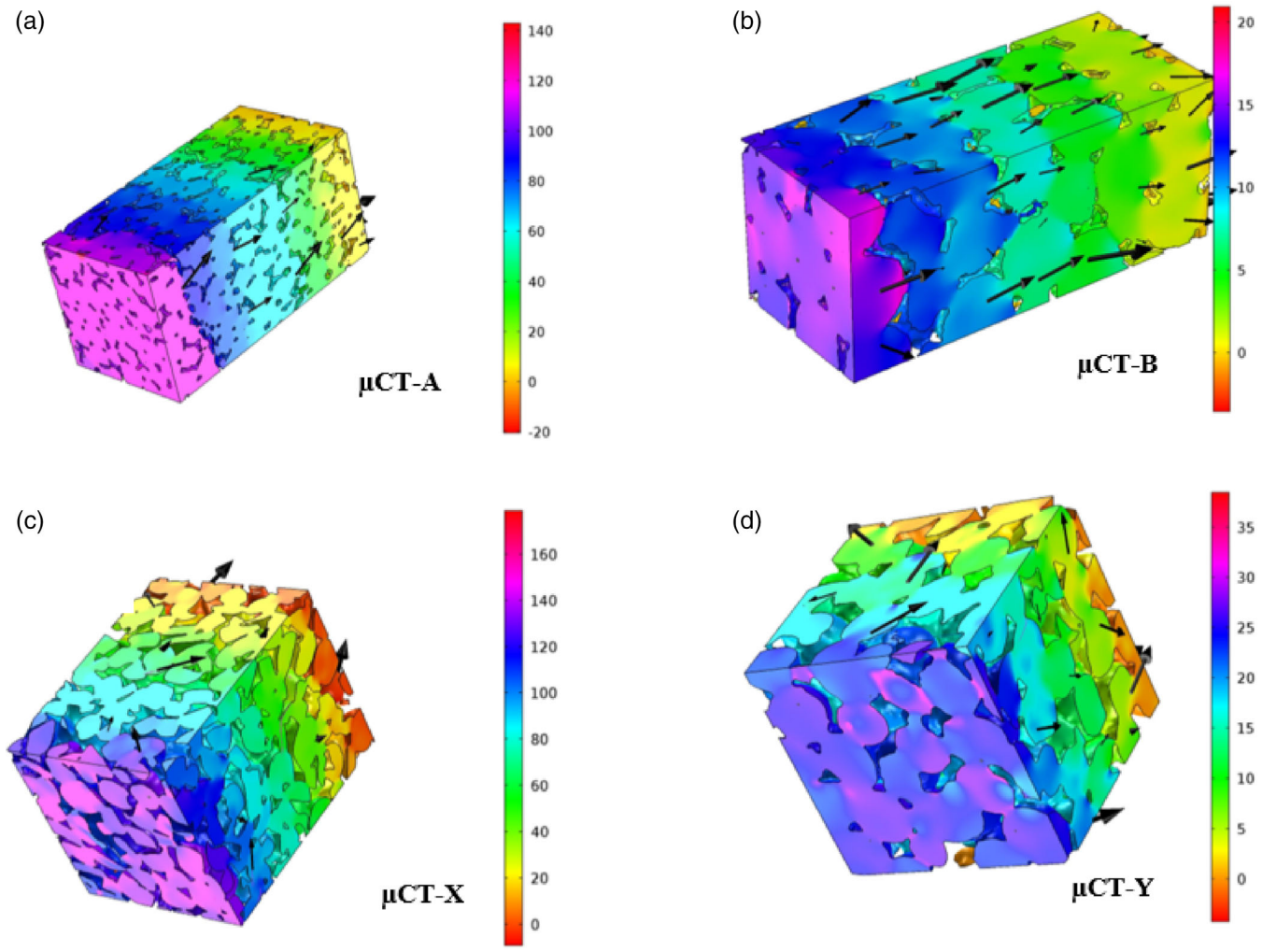

FIGURE 5 Three-dimensional representative elemental volume of pressure profile arrow/streamline plots (Pa) at 1 m s^{-1} superficial fluid inlet velocity for the Inconel foam samples: (a) 450 μm (μCT-*A*) and (b) 1,200 μm (μCT-*B*) and the *bottleneck-type* porous metallic samples: (c) μCT-*X* and (d) μCT-*Y*. μCT, X-ray micro-computed tomography [Color figure can be viewed at wileyonlinelibrary.com]

lower pressure drop values. This is an indication that porous metallic structures characterized by low pore-openings offer greater resistance to slow-moving fluid in the Darcy regime while low-pore volume structures offer a higher resistance to fast-moving fluid, typically in the laminar and turbulent flow regimes. Table 1 shows that the pore-volume fraction has an inverse relationship to the specific surfaces of the porous structures. Optical and X-ray CT imaging of the Inconel structures revealed that lower pore volumes are associated with structures characterized by larger ligaments (struts) which convey the moving fluid into the pore spaces provided by the structures. In the case of the *bottleneck-type* Al foams, the near-circular pore wall geometry provided by the higher-porosity (μCT-*Y*) structures are smaller in size compared to the low-porosity μCT-*X* foam. The large size cell walls provided by the lower-porosity foam offers greater resistance to moving fluid. Experimental methodology on the processing of these Al foams by a replication-casting approach[22,36,40] described the pore-volume and pore-openings of *bottleneck-type* foams to be mainly dependent on the packing density and applied infiltration used during casting of the sample. The replication casting process requires that liquid metal is poured into a cylindrical vessel consisting of packed beds of porogens (salt beads). The salt beads are initially heated to a temperature between 450 and 600°C to avoid premature solidification of the melt. The depth of penetration of the liquid melt into the beds is dependent on the applied differential pressure used to drive the melt into the convergent spaces provided by the packed bed. Higher differential pressures (typically, 1 bar or more) often result in structures with fewer and less openings while low applied differential pressure would likely yield structures with higher pore openings. A mathematical relationship (Laplace equation) describing this infiltration pressure as a function of capillary radius, surface tension and wetting angle provided by the packed beds during replication casting, is provided in References 26 and 44. Also, low porosity and higher porosity *bottleneck-shaped* cellular structures are associated with loose and densely packed beds of near-spherical structures, respectively. In other words, a loosely packed bed promotes larger pore spaces (40–48%) for the liquid melt; when solidified and the salt removed (by dissolution in a

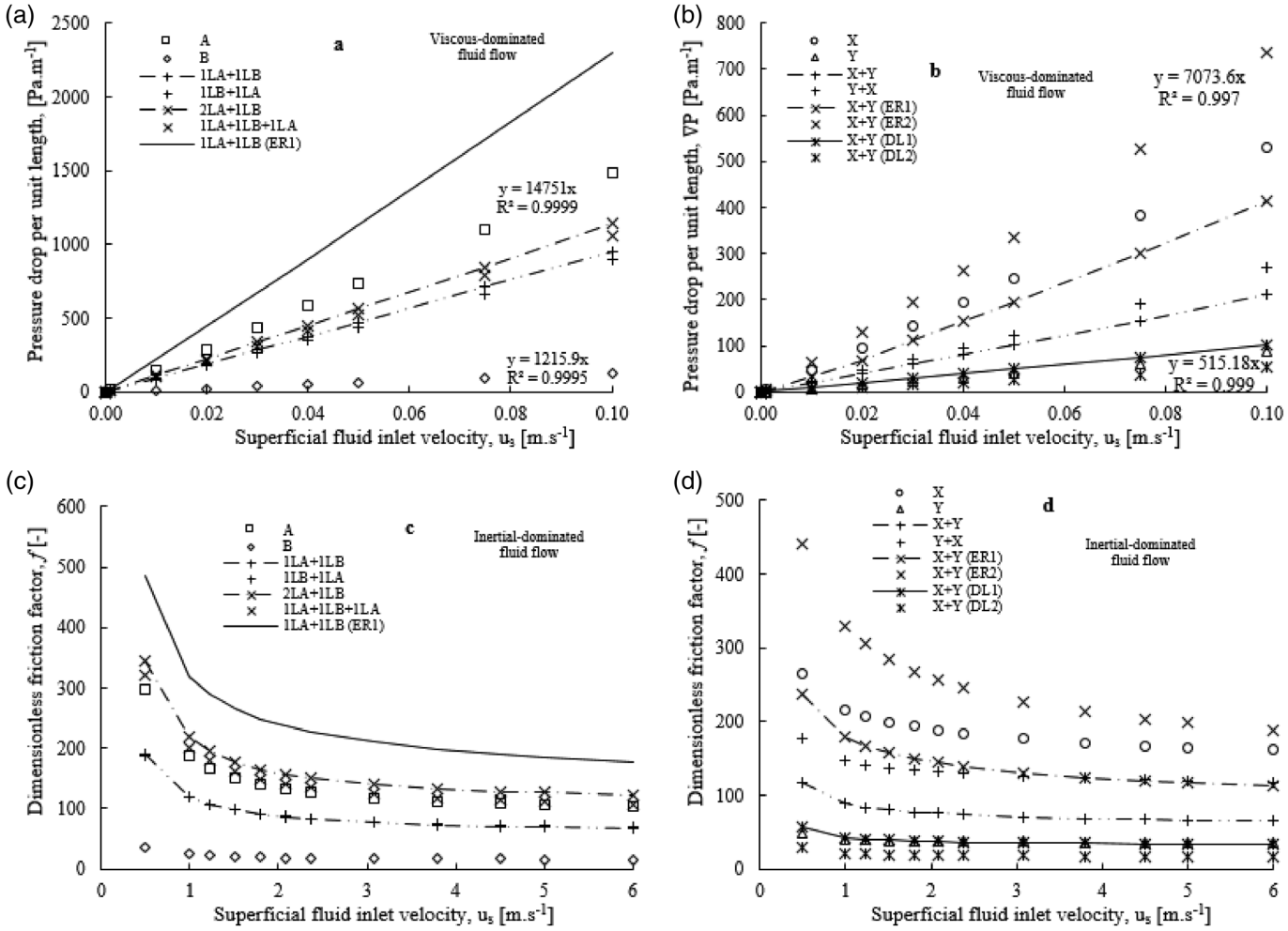

FIGURE 6 Graphical representations of flow information: (a) viscous-dominated unit pressure drop, ∇P (Pa m^{-1}) against superficial fluid velocity, u_s (m s^{-1}) for single and stacked samples of Inconel foams. (b) Viscous-dominated unit pressure drop, ∇P (Pa m^{-1}) against superficial fluid velocity, u_s (m s^{-1}) for the *bottleneck-type* aluminum foams, (c) inertial-dominated dimensionless friction factor, f (–) against superficial fluid inlet velocity, u_s (m s^{-1}) for single and stacked samples of Inconel foams, and (d) inertial-dominated dimensionless friction factor, f (–) against superficial fluid inlet velocity, u_s (m s^{-1}) for single and stacked samples of *bottleneck-type* aluminum foams

warm incubator bath [35–40°C] for 72 hr[23]), the replicated porous matrix would provide a higher surface area and lower pore volume for flowing fluid. In contrast, densely packed beds offer fewer pore spaces (33–38%) for infiltrated liquid melt; when solidified and salt removed, this structure is more likely to provide a lower surface area, which allows moving fluid to fully penetrate its architecture.

Analysis of the behavior of fluid flow across stacked samples of microcellular structures is made possible by plotting the viscous-dominated unit pressure drop and inertial-dominated dimensionless friction factor against their superficial fluid inlet velocities, as shown in Figure 6. Figure 6a,b presents the viscous-dominated unit pressure drop against superficial fluid velocity for the single and stacked samples of Inconel and Al foams, respectively. Also, Figure 6c,d presents the inertial-dominated friction factor for the Inconel and Al single and stacked samples, respectively. These figures also show the viscous-dominated and inertial-dominated fluid flow behavior across structural-adapted (erosion [ER] and dilation [DL]) structures. The term erosion in this work simply implies the removal of voxel elements from the fluid phase 3D REV real sample, thereby, resulting in a low-porosity structure that bears a facsimile of the real sample. In contrast, dilated samples are obtained by the addition of voxel elements to the fluid phase of the 3D REV real sample, hence, resulting in highly porous samples. The terms 1, 2, and 3 in Table 1 simply indicate the number of pixel elements. It is noteworthy to remention that the voxel sizes for the Inconel and Al foams are 12 and 26 μm, respectively. Unit pressure drop and dimensionless friction factor were, respectively, lowest and highest for extremely dilated and eroded samples. This can be attributed to the changes in the pore-structure-related properties of the adapted structures in comparison with the real ones. Table 1 palpably shows that the pore-openings and pore-volume fraction are higher for the 3D REV real samples when compared to the 3D REV-eroded samples, thereby yielding very high-pressure drop values. Similarly, the pore-structure-related properties are higher for the dilated samples, hence, a gradual decline in the

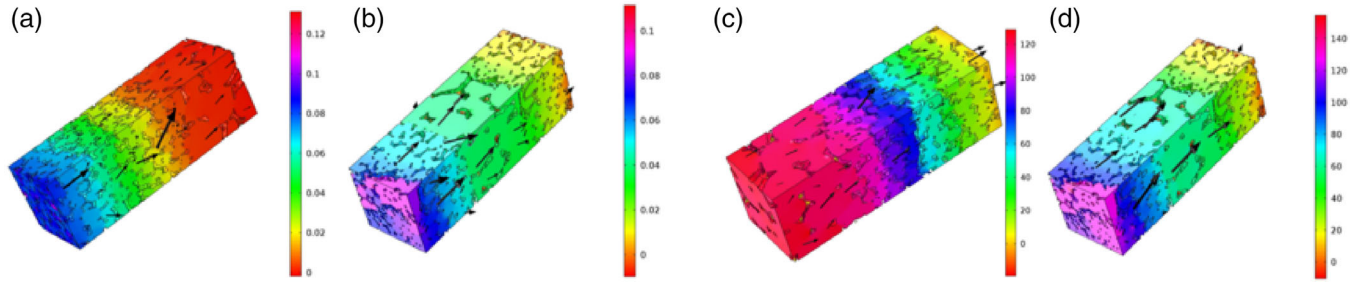

FIGURE 7 Three-dimensional pressure profile plots for stacked samples of the Inconel (μCT-*A* and μCT-*B*) foams (a) 2LA + 1LB at u_s=10^{-3} m s^{-1}, (b) LA + LB + LA at u_s=10^{-3} m s^{-1}, (c) 1LB + 2LA at u_s=1 m s^{-1}, and (d) LA + LB + LA at u_s=1 m s^{-1}. μCT, X-ray micro-computed tomography. LA, thickness of sample A; LB, thickness of sample B [Color figure can be viewed at wileyonlinelibrary.com]

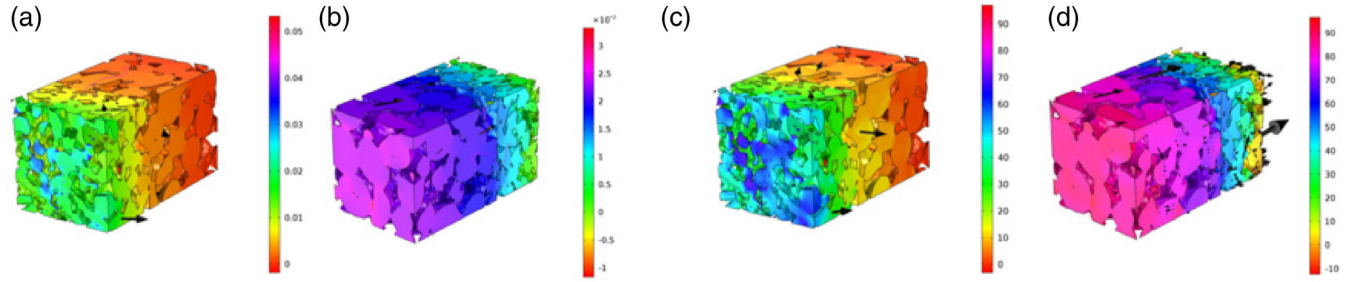

FIGURE 8 Three-dimensional pressure profile plots for stacked samples of the *bottleneck-type* porous metallic structures (μCT-*X* and μCT-*Y*) (a) *X* + *Y* at u_s=10^{-3} m s^{-1}, (b) *Y* + *X* at u_s=10^{-3} m s^{-1}, (c) *X* + *Y* at u_s=1 m s^{-1} and (d) *Y* + *X* at u_s=1 m s^{-1}. μCT, X-ray micro-computed tomography [Color figure can be viewed at wileyonlinelibrary.com]

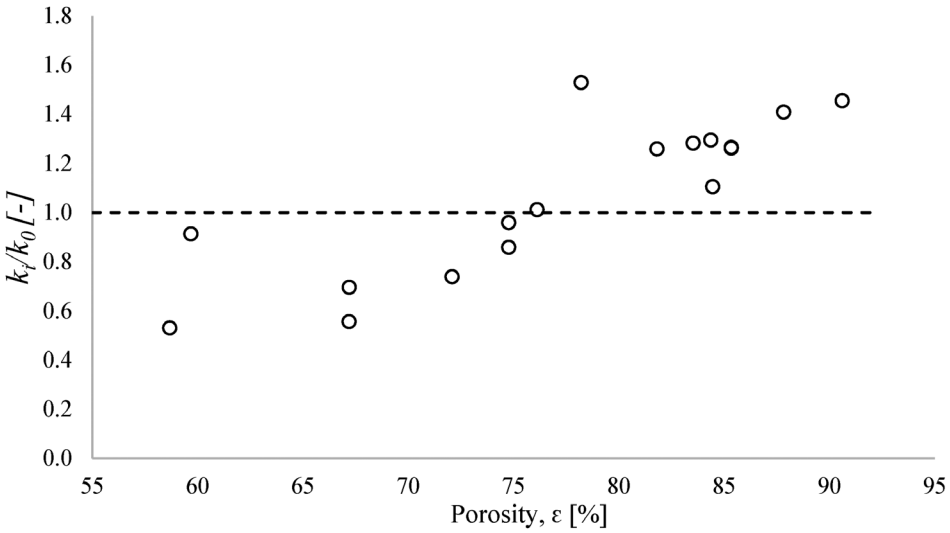

FIGURE 9 A graphical representation of the permeability ratio against porosity of the porous structures

resistance offered by these adapted samples results in an increase in their flow permeability.

Figures 7 and 8 present 3D REV streamline/arrow pressure plots for the stacked samples of Inconel and Al foams for superficial fluid inlet velocity of 10^{-3} m s^{-1} (slow-moving fluid) and 1.0 m s^{-1} (fast-moving fluid). Flow parameters for the stacked samples of Inconel and Al foam structures lie within the flow behavior developed across individual low and high porosity real samples (Figures 6–8). The increased pore density of the Inconel 450 μm foam in stacked samples of the Inconel foams, Figure 7a, results in very a high-pressure drop value as well as increased frictional forces exerted between the moving fluid and pore cell walls (Figure 6a,c). Table 1 shows that there are little, or only insignificant changes in the computed fluid flow data obtained for the stacked samples of all the porous structures for low fluid velocities, irrespective of their flow entrances length. This, therefore, confirms the hypothesis that flow permeability of porous structures is mainly dependent on pore morphological features at Darcy regime.[4,14]

However, this statement is relatively untrue for high fluid flow in

stacked samples for microcellular structures. Flow entrance through the low pore density (larger pore sizes) to the high pore density (smaller pore sizes) in stacked samples yields a higher pressure drop with increasing flow resistance (Form drag). An assessment of the 3D REV pressure plots shows that higher pressure drops are recorded at flow compression zones (sudden compression, Figure 8d) than at sudden expansion zones (Figure 8c). In other words, the resistance offered by the subsequent samples with low porosity (or low pore size) structures results in forced recirculation with particle interaction of the flowing fluid confined to the pore spaces provided by the porous matrices. The pressure drop in stacked samples preceded by lower pore size material is relatively low, thus, a relaxation in the flow eddies (low particle interaction) and a smooth transition of the moving fluid into larger pore spaces provided by the succeeding sample is seen (Figures 6c,d and Table 1).

Experimental measurements[8,19] and μCT-based CFD modeling and simulation[4] of pressure drops across high porosity (0.78–0.94) porous metallic structures showed that inertial-dominated flow permeabilities (k_i) were higher than flow permeabilities (k_0) for slow-moving fluid in the Darcy regime. Figure 9 agrees with this statement for high porosity materials, typically, beyond 76%. However, further investigations into the flow permeabilities of low porosity materials (ε < 76%) proved otherwise. This can be attributed to the reduced pore openings characterized for these structures (Table 1), thereby offering high resistance to a fast-moving fluid, most especially, at the entrance point. During flow studies, the pore-structure-related information and topology of the porous materials remain unchanged even at high fluid flow rates, but, the ability of the moving fluid to fully penetrate the surface topology of high-porosity foams is evident for inertial-dominated fluid flow.[4,19] However, these observations for the flow permeabilities of the low-porosity structures were based solely on the recorded flow data obtained via μCT-based CFD modeling and simulation and would require several experimental investigations of pressure drop across a wide range of low porosity foams to support this claim.

4 | CONCLUSIONS

X-ray CT-based CFD modeling and simulation of fluid flow behavior in single and stacked samples of Inconel and Al foams have been presented with tolerable agreement to experimental results. The results of pressure drop data developed across porous samples restrict viscous-dominated and inertial-dominated fluid regimes to a superficial fluid velocity below and above 0.1 m s^{-1}, respectively. Flow permeability and Form drag dependence on pore-structure-related properties are described for both cases of very slow and fast-moving fluids. The pore-level CFD approach enables a deep understanding of the flow laws at the interstices of the porous matrices. Deductions from the effective transport properties indicate that pore-openings are imperative for describing the behavior of slow moving fluids, typically, in the Darcy regime while changes in pore-volume fraction are key to understanding the behavior of a fast-moving fluid. Relative contributions of the changes in pore-morphological features of stacked samples on the estimated permeability and Form drag values are also described.

ACKNOWLEDGMENTS

Dr. AJ would like to acknowledge the University of Nottingham Dean's Award (Nottingham, UK), Petroleum Technology Development Fund (Abuja-Nigeria), Synopsis-Simpleware Ltd (Los Angeles, CA), Bowers and Wilkins Group (West Sussex, UK), and Prof. Andrew R. Kennedy (Lancaster University, UK) for the provision of porous metallic structures, X-ray tomography scans, funds, licenses, and technical support.

ORCID

Abdulrazak J. Otaru https://orcid.org/0000-0002-3057-4991

REFERENCES

1. Vicente J, Brun E, Hugo JM, Bonnet JP, Topin F. Determination of effective transport properties of metallic foams: morphology and flow laws. *Single and Two-Phase Flows on Chemical and Biomedical Engineering*. USA: Bentham Science Publishers, Ltd; 2011.
2. Edouard D, Lacroix M, Pham C, Mbodji M, Pham-Huu C. Experimental measurements and multiphase flow models in solid SiC foam beds. *AIChE J*. 2008;54(11):2823-2832.
3. De Carvalho TP, Morvan HP, Hargreaves D, Oun H, Kennedy A. Pore-scale numerical investigation of pressure drop behaviour across open-cell metal foams. *Tran Porous Med*. 2017;117:311-336. https://doi.org/10.1007/s11242-017-0835-y.
4. Otaru AJ. The permeability of replicated microcellular structures in the Darcy regime. *Am Inst Chem Eng AIChE J*. 2020;66. https://doi.org/10.1002/aic.16915.
5. Otaru AJ, Morvan HP, Kennedy AR. Modelling and optimisation of sound absorption in replicated microcellular metals. *Scr Mater*. 2018;150:152-155.
6. Lu JJ, Hess A, Ashby MF. Sound absorption of metallic foams. *Am Inst Phys*. 1999;99:07511-9.
7. Ashby MF, Evans A, Kennedy AR. The role of oxidation during compaction on the expansion and stability of Al foams made via a PM route. *Adv Eng Mater*. 2006;8:568-570.
8. Oun H, Kennedy AR. Tailoring the pressure drop in multi-layered open-cell porous Inconel structures. *J Porous Mater*. 2015;2:1627-1633.
9. Dukhan N. Metal foams: fundamentals and applications, DESTECH publication, Inc. technology and engineering, USA. *Pp*. 2013;3-127.
10. Otaru AJ. Review on the acoustical properties and characterisation methods of sound absorbing porous structures: a focus on microcellular structures made by a replication casting method. *Met Mater Int*. 2019;26:915-932. https://doi.org/10.1007/s12540-019-00521-y.
11. Bekaert Group, *Porous Metals Filter Elements and Systems for Liquids*. 2013, DEStech Publications Inc., USA. www.bekaert.com. 25th November 2019.
12. Yang XH, Kuang JJ, Lu TJ, Han FS, Kim T. A simplistic analytical unit cell based model for the effective thermal conductivity of high porosity open-cell metal foams. *J Phys D*. 2013;46:255302.
13. Otaru AJ, Fluid Flow and Acoustic Absorption in Porous Metallic Structures using Numerical Simulation and Experimentation [PhD thesis]. Nottingham, UK: The University of Nottingham; 2018.
14. Dybbs A, Edwards RV. A new look at porous media fluid mechanics—Darcy to turbulent. In: Bear MY, Corapcioglu MY, eds. *Fundamentals of Transport Phenomena in Porous Media*. NATO ASI Series (Series E: Applied Sciences). Vol 82. Dordrecht: Springer; 1984.

15. Ranut P, Nobile E, Mancini L. High resolution microtomography-based CFD simulation of flow and heat transfer in aluminium metal foams. *Appl Therm Eng*. 2014;69(2):230-240.
16. Gunjal PR, Ranade VV, Chaudhari RV. Computational study of a single-phase flow in packed beds of spheres. *AIChE J*. 2005;51:365-378.
17. Guo X, Dai R. Numerical simulation of flow and heat transfer in a random packed bed. *Particuology*. 2009;8:293-299.
18. Dorai F, Teixeira MC, Rolland M, Climent E, Marcoux M, Wachs A. Fully resolved simulations of the flow through a packed bed of cylinders: effect of size distribution. *Chem Eng Sci*. 2015;129:180-192.
19. Oun H, Kennedy AR. Experimental investigation of pressure drop characterization across multilayer porous metal structure. *JPorous Mater*. 2014;21:1133-1141.
20. Dukhan N, Patel P. Equivalent particle diameter and length scale for pressure drop in porous metals. *Exp Therm Fluid Sci*. 2008;32:1059-1067.
21. Weber L, Ingram D, Guardia S, Athanasiou-Ioannou A, Mortensen A. Fluid flow through replicated microcellular materials in the Darcy–Forchheimer regime. *Acta Mater*. 2017;126:280-293.
22. Otaru AJ, Morvan HP, Kennedy AR. Measurement and simulation of pressure drop across replicated microcellular aluminium in the Darcy–Forchheimer regime. *Acta Mater*. 2018;149:265-275.
23. Bouhouch A, Prat M, Boisson H. Variable density flow in porous media: a study by means of pore level numerical simulations. *Int J Num Methods Fluids*. 1999;30:725-742.
24. Della Torre A, Montenegro G, Tabor GR, Wears ML. CFD characterization of flow regimes inside open cell foam substrates. *Int J Heat Fluid Flow*. 2014;50:72-82.
25. Della Torre A, Lucci F, Montenegro G, et al. CFD modelling of catalytic reactions in open-cell foam substrates. *Comput Chem Eng*. 2016;92:55-63.
26. Otaru AJ, Kennedy AR. The permeability of virtual macroporous structures generated by sphere-packing models: comparison with analytical models. *Scr Mater*. 2016;124:30-33.
27. Ranut P, Nobile E, Mancini L. Microtomography-based CFD analysis of transport in open-cell aluminium metal foams. *J Phys Conf Ser*. 2014;501:012021.
28. Watson IG, Lee PD, Dashwood RJ, Young P. Simulation of the mechanical properties of an aluminium matrix composite using X-ray micro-tomography. *Metal Mater Trans*. 2006;37A:551-558.
29. Petrasch J, Wyss P, Stampili R, Steinfeld A. Tomography-based multiscale analysis of the 3D geometrical morphology of reticulated porous ceramics. *JAm Ceram Soc*. 2008;91(8):2659-2665.
30. Ghazi A, Berke P, Ehab Moustafa Kamel K, Sonon B, Tiago C, Massarat TJ. Multiscale computational modelling of closed-cell metallic foams with detailed microstructural morphological control. *Int J Eng Sci*. 2019;143:92-114.
31. Otaru AJ. Enhancing the sound absorption performance of porous metals using tomography images. *Appl Acoust*. 2019;143:183-189.
32. Diani A, Bodla KK, Rossetto L, Garimella SV. Numerical investigation of pressure drop and heat transfer through reconstructed metal foams and comparison against experiments. *Int J Heat Mass Trans*. 2015;88:508-525.
33. Nie Z, Lin Y, Tong Q. Numerical investigation of pressure drop and heat transfer through open-cell foams with 3D Laguerre–Voronoi model. *Int J Heat Mass Trans*. 2017;113:819-839.
34. Zafari M, Panjepour M, Emami MD. Microtography-based numerical simulation of fluid flow and heat transfer in open cell metal foams. *Appl Therm Eng*. 2015;80:347-354.
35. Lucci F, Della Torre A, Montenegro G, Kaufmann R, Eggenschwiler PD. Comparison of geometrical, momentum and mass transfer characteristics of real foams to kelvin cell lattices for catalyst applications. *Int J Heat Mass Trans*. 2017;108:341-350.
36. Kennedy, AR, Porous Metals and Metal Foams Made from Powders, Powder Metallurgy, IntechOpen, Rijeka, 2012, *Katsuyoshi Kondoh*, Chapter 2, https://doi.org/10.5772/33060
37. Carmignato S, Dewulf W, Leach R. *Industrial X-Ray Computed Tomography*. Gewerbestrasse, Switzerland: Springer International Publishing AG; 2018.
38. Fan X, Ou X, Xing F, et al. Microtomography-based numerical simulations of heat transfer and fluid flow through β-SiC open-cell foams for catalysis. *Catalysis Today*. 2016;278(2):350-360.
39. Lage JL, Krueger PS, Narasimham A. Protocol for measuring permeability and form coefficient of porous media. *Phys Fluids*. 2005;17:088101.
40. Otaru AJ, Morvan HP, Kennedy AR. Airflow measurement across negatively-infiltration processed porous aluminium structures. *AIChE J*. 2019;65:1355-1364.
41. Bonnet JP, Topin F, Tadrist L. Flow laws in metal foams: compressibility and pore size effects. *Trans Porous Med*. 2008;73:149-163.
42. Boomsma K, Poulikakos D, Ventikos Y. Simulations of flow through open cell metal foams using idealized periodic cell structure. *Int J Heat Fluid Flow*. 2003;24(6):825-834.
43. Otaru AJ, Morvan HP, Kennedy AR. Numerical modelling of the sound absorption spectra for bottleneck dominated porous metallic structures. *Appl Acoust*. 2019;151:164-171.
44. Langston P, Kennedy AR. Discrete element modelling of the packing of spheres and its application to the structure of porous metals made by infiltration of packed beds of NaCl beads. *Powder Technol*. 2014;268:210-218.

How to cite this article: Otaru AJ, Abdulkadir M, Corfield MR, Kenfack A, Tanko N. Computational evaluation of effective transport properties of differential microcellular structures. *AIChE J*. 2020;e16928. https://doi.org/10.1002/aic.16928